

ToddlerDiffusion: Flash Interpretable Controllable Diffusion Model

Eslam Mohamed Bakr¹, Liangbing Zhao¹, Vincent Tao Hu²,
Matthieu Cord³, Patrick Perez³, Mohamed Elhoseiny¹

¹KAUST ²LMU ³VALEO AI

Abstract

Diffusion-based generative models excel in perceptually impressive synthesis but face challenges in interpretability. This paper introduces ToddlerDiffusion, an interpretable 2D diffusion image-synthesis framework inspired by the human generation system. Unlike traditional diffusion models with opaque denoising steps, our approach decomposes the generation process into simpler, interpretable stages—generating contours, a palette, and a detailed colored image. This not only enhances overall performance but also enables robust editing and interaction capabilities. Each stage is meticulously formulated for efficiency and accuracy, surpassing Stable-Diffusion (LDM). Extensive experiments on datasets like LSUN-Churches and COCO validate our approach, consistently outperforming existing methods. ToddlerDiffusion achieves notable efficiency, matching LDM performance on LSUN-Churches while operating three times faster with a 3.76 times smaller architecture. Our source code is provided in the supplementary material and will be publicly accessible.

1. Introduction

In recent years, diffusion models [18, 47, 49] have made significant strides across diverse domains, revolutionizing image synthesis and related tasks by transforming noisy, unstructured data into coherent representations through incremental diffusion steps [10, 18, 37, 41]. Their versatility extends beyond image generation to tasks such as image denoising [15, 25, 60], inpainting [1, 33], super-resolution [12, 27], and applications in 3D content creation [2, 40, 43], data augmentation [5, 29, 53], medical imaging [6, 21, 56, 57], anomaly detection, and more.

Despite their success in high-quality image generation without adversarial training, diffusion models encounter limitations: (1) the need for numerous steps to produce a sample, (2) lack of interpretability in intermediate steps, and (3) substantial training time requirements. Various solvers and samplers have been proposed to address slow sampling [28, 32, 48], but these solutions primarily focus on sampling

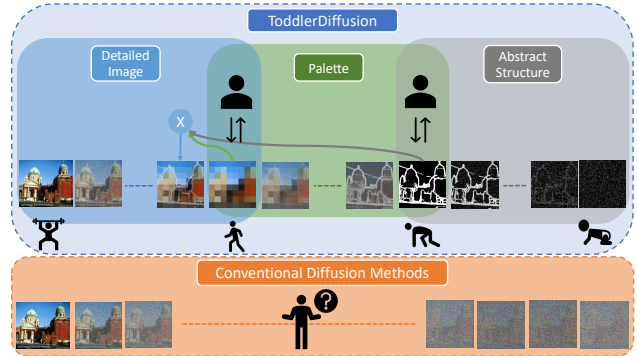


Figure 1. At the top is an overview of our proposed pipeline, termed ToddlerDiffusion. First, we unconditionally generate an abstract structure; coarse contours. Secondly, starting from the coarse structure we generate tentative palette that matches this structure. Then, we overlay the output from both stages.

efficiency without addressing training efficiency or the core issue of slow sampling. In response, we propose a new generation pipeline, ToddlerDiffusion, designed to overcome these limitations in diffusion-based models.

Our approach introduces an interpretable generation pipeline by decomposing the complex RGB generation task into a series of interpretable stages, inspired by the human generation system [34, 35, 50]. Unlike traditional models that generate the complete image in one complex stage, we break it down into N simpler stages, starting with abstract contours, followed by an abstract palette, and concluding with the detailed RGB image. This decomposition not only enhances interpretability but also facilitates dynamic user interaction, offering unprecedented editing capabilities for unconditional generation, as shown in Figure 2. In addition, our framework is versatile, compatible with any conditional framework, such as label-conditioning and text conditioning. The decomposition of the generation process into simpler components enables the use of more compressed networks for each subtask, resulting in a more efficient overall architecture. Our hypothesis posits that breaking down the generation task into simpler stages accelerates both sampling and training processes by utilizing smaller architectures for each stage. Additionally, our design inherently reduces the need for extensive denoising steps during both training and sampling. Leveraging the Schrödinger

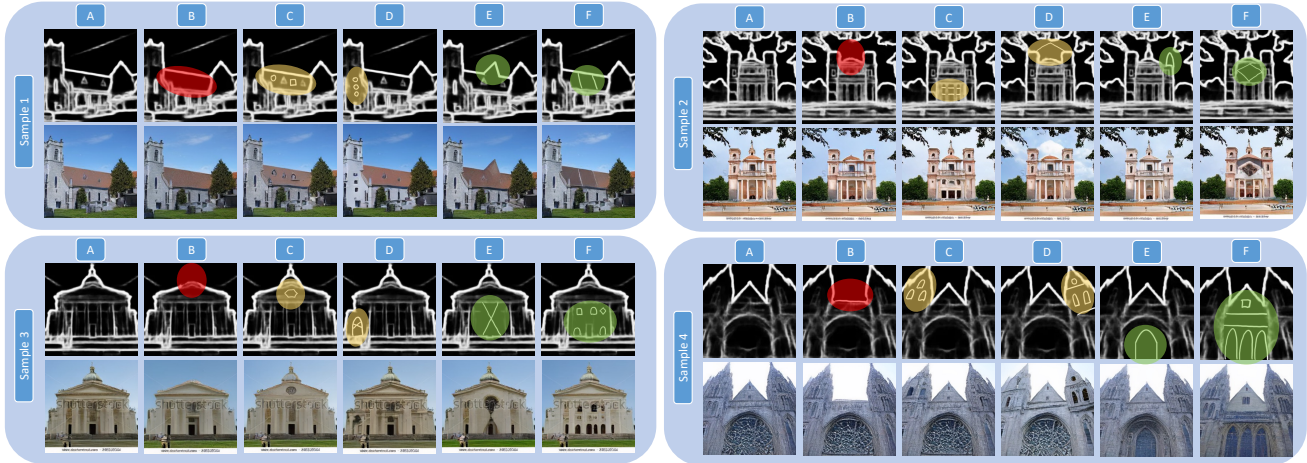


Figure 2. Controllability ability of our framework, ToddlerDiffusion. Starting from generated sketch and RGB image (A), we can remove artifacts or undesired parts, in red, (B), add a new content, in yellow, (C-D), and edit the existing content, in green, (E-F) by manipulating the sketch.

Bridge [26, 54] to model all stages, our approach achieves these advancements without relying on manual ground truth annotations, employing human-free guidance for enhanced efficiency and practical applicability. To evaluate our proposed framework, we conduct comprehensive experiments on two datasets: LSUN-Churches [58], and COCO [30], covering unconditional, class-label conditioning, and text conditioning scenarios. For sketch generation, we outperform LDM’s performance with a $41\times$ smaller network. In RGB generation, we surpass LDM by 4.5 FID score points with the same complexity and achieve a 2 FID score point improvement while being $2.5\times$ faster. Our contributions can be succinctly summarized as follows:

- We introduce an inherently interpretable and controllable diffusion model, denoted as ToddlerDiffusion, that systematically generates a chain of interpretable stages leading to the final image.
- Providing robust editing and interaction capabilities for both conditional and unconditional generation scenarios.
- Our pipeline is capable of training a diffusion model from scratch using a minimal number of steps (10).
- Our approach achieves state-of-the-art results in challenging setups, where both training and sampling are performed with a limited number of steps (10-20).
- We surpass all existing efficient diffusion-based methods, demonstrating superior performance in terms of training and sampling time, as well as overall model performance.

2. Revisiting Diffusion Models

2.1. Preliminaries

Diffusion models [18, 47, 49] progressively transform a sample \mathbf{x}_0 originating from a natural data distribution $\mathbf{x}_0 \sim q(\mathbf{x})$ into a noisy variant \mathbf{x}_t , i.e., forward process, where $t \in [1, T]$ and T is the total number of the steps. The for-

ward process [18] could be formulated by:

$$q(\mathbf{x}_t | \mathbf{x}_0) = \mathcal{N}(\mathbf{x}_t; \sqrt{\bar{\alpha}_t}\mathbf{x}_0, (1 - \bar{\alpha}_t)\mathbf{I}), \quad (1)$$

where, σ_t^2 is the variance schedule, $\alpha_t = 1 - \sigma_t^2$ and $\bar{\alpha}_t = \prod_{i=1}^t \alpha_i$. Then, the goal is to learn the inverse mapping $q(\mathbf{x}_{t-1} | \mathbf{x}_t)$ to be able to sample real data \mathbf{x}_0 given a Gaussian noise \mathbf{x}_T , i.e., reverse process. However, this conditional probability is not tractable, therefore, we approximate it using a model $p_\theta(\mathbf{x}_{t-1} | \mathbf{x}_t)$, where θ represents the network parameters. The learning objective is the Variational Lower Bound (ELBO):

$$\begin{aligned} \mathcal{L}_{ELBO} = & -\mathbb{E}_q(D_{KL}(q(x_T|x_0)||p(x_T))) \\ & + \sum_{t=2}^T D_{KL}(q(x_{t-1}|x_t, x_0)||p_\theta(x_{t-1}|x_t)) \\ & - \log p_\theta(x_0|x_1), \end{aligned} \quad (2)$$

where the reverse process [18] is formulated as:

$$q(x_{t-1} | x_t, x_0) = \mathcal{N}(x_{t-1}; \tilde{\mu}(x_t, x_0), \tilde{\sigma}_t^2 \mathbf{I}) \quad (3)$$

2.2. Limitations

Interpretability Diffusion-based methods lack interpretability in their denoising steps, making it challenging to understand the rationale behind the model’s final image generation. The hidden transformations in intermediate steps lack specific semantic meaning, hindering the attribution of contributions to overall image content [7].

Controllability The inherent lack of interpretability in diffusion-based methods limits controllability during image generation. Users struggle to exert direct control over specific attributes or features due to intricate denoising step transformations. To address this, we decompose the generation problem into multiple stages (Figure 4), creating a

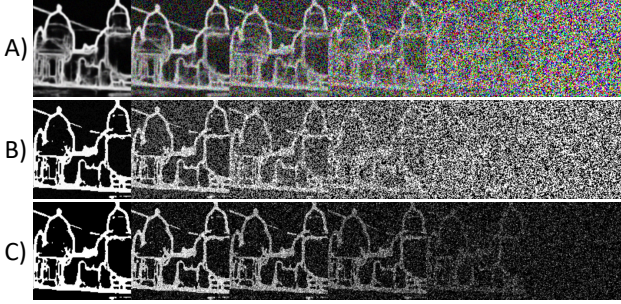


Figure 3. Comparison between different formulations for the 1st stage. This depicts the forward process for each formulation.

Chain-of-Thoughts (CoT) framework. CoT enables real-time monitoring and intervention in the generation process for full control [20].

Training time Current diffusion-based models suffer from prolonged training times, hampering their applicability, especially in resource-intensive tasks like video generation. This extended training period poses financial and environmental challenges. In contrast, our framework, ToddlerDiffusion, achieves comparable performance to LDM on the LSUN-Churches dataset while being three times faster and using a 3.76 times smaller architecture.

3. ToddlerDiffusion

We introduce ToddlerDiffusion, an approach that strategically decomposes the RGB generation task into simpler and more manageable subtasks based on modalities, such as sketch/edge and palette. First, Section 3.1 elaborates on our formulation for each stage. By decomposing the generation process into simpler components, our model not only becomes interpretable but also empowers users to interact with the system dynamically (Section 3.2), as illustrated in Figure 1. Significantly, our approach achieves these advancements without relying on manual ground truth annotations, instead leveraging human-free guidance for enhanced efficiency and practical applicability (Section 3.3).

3.1. Toddler Growth

The development of our method was inspired from child’s growth, where the learning process in their brains is decomposed into stages and developed step-by-step. By analogy, we decompose the 2D image synthesis into different, more straightforward stages. In this section, we will dissect each stage. Then, in the following sections, we will demonstrate the benefits of our novel formulation.

1st Stage: Abstract Structure. This stage aims to generate abstract contours $\mathcal{S} \in \mathbb{R}^{H \times W \times 3}$ starting from just pure noise (unconditional generation) or a condition, e.g., label or text. One possible solution is to utilize the original diffusion formulation, Eq. 1 and Eq. 3. However, this is not aligned with the sketch nature, as shown in Figure 3, case A.

On the contrary, we formulate a unique formulation tailored for sketch generation. First, we replaced the Gaussian distribution with the Bernoulli distribution, as shown in case B Figure 3, a discretized version of the Gaussian distribution. However, this is not optimized enough for the sparsity nature of the sketch, where less than 20% of the sketch is white pixels. More specifically, we are starting from a pure noise distribution \mathbf{x}_T and want to learn the inverse mapping $q(\mathbf{x}_{t-1} | \mathbf{x}_t)$ to be able to sample real data \mathbf{x}_0 . The issue is located in the vast gap between the two domains: \mathbf{x}_T and \mathbf{x}_0 . Following [22], this can be interpreted as signal-to-noise ratio (SNR), where $\text{SNR}(t) = \frac{\alpha_t}{\sigma_t^2}$. Following Eq. 1:

$$\text{at } t = T \rightarrow \alpha_T = 0 \quad \therefore \text{SNR}(T) = 0.$$

To fill this gap, we formulate the unconditional sketch generation as a bridge [26, 31, 38, 54], where we learn the mapping function from domain $y = x_T$ to domain $x = x_0$. Our forward process can be formulated as follows:

$$x_t = \alpha_t \mathcal{F}_d(x_0, t) + (1 - \alpha_t)y + \sigma_t^2 \epsilon_t, \quad (4)$$

where α_t is a weighting factor between the two domains, σ_t^2 is the noise variance, and $\mathcal{F}_d(x_0, t)$ is dropout function that takes the GT sketch x_0 and the current time-step t and generate more sparse version of x_0 by masking some white pixels, where larger t leads to more aggressive masking. In the conventional DDPM [18] and LDM [44], y is Gaussian distribution which leads to the huge gap ($\text{SNR}(T) = 0$). In contrast, we set y as a black image, $y \in \mathbb{R}^{H \times W \times 3}$, and use a linear noise schedule $\sigma_t^2 = 1 - \alpha_t$, as shown in the top part of Figure 4. To align our design with the sketch nature, as shown in Figure 7, part C, we add a gray noise as generating a 1-dimensional sketch is sufficient and set the variance peak at x_T to a small number, due to the sparsity of the sketch. In other words, the added brighter points on the black canvas act as control points during the progressive steps ($T \rightarrow 0$) while converging to form the contours, as shown in Figure 7, part C.

2nd Stage: Palette. Once we generate the sketch $\mathcal{S} \in \mathbb{R}^{H \times W \times 3}$, one possible solution is to directly feed it into the 3rd stage, i.e., detailed image generation. However, we can optionally add another intermediate stage to generate color information, represented by a palette as shown in Figure 1, which introduces more guidance for the last stage, in addition to invoking more interpretability and controllability for the generation pipeline. Following the same formulation from the 1st stage, Eq. 4, we define the forward process as an image-to-image translation and formulate the problem using the schrödinger bridge [26, 54]. Our forward process can be seen as follows:

$$x_t = \alpha_t \mathcal{F}_p(x_0, \mathcal{K}_t, \mathcal{J}_t) + (1 - \alpha_t)y + \sigma_t^2 \epsilon_t, \quad (5)$$

$$\sigma_t^2 = \alpha_t - \alpha_t^2, \quad (6)$$

where α_t is a weighting factor between the two domains, σ_t^2 is the noise variance, and $\mathcal{F}_p(x_0, \mathcal{K}_t, \mathcal{J}_t)$ is a pixilation

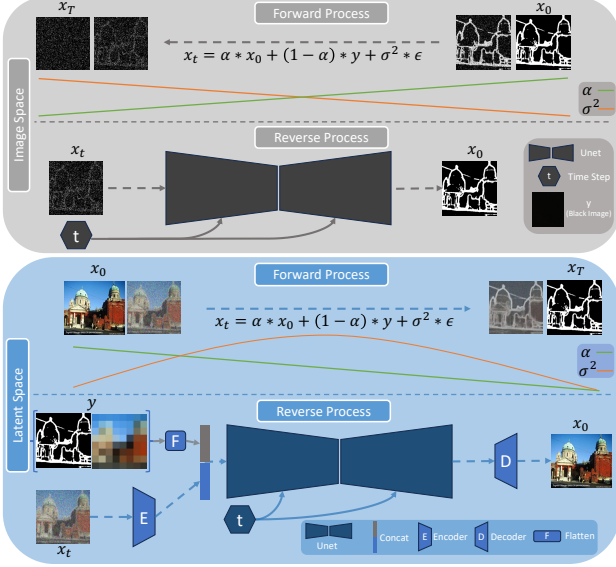


Figure 4. An overview of proposed architecture, dubbed ToddlerDiffusion. The first block demonstrates the first stage which generates a sketch unconditionally. Due to our efficient formulation, this stage operates in the image space on 64×64 resolution. The bottom module depicts the third stage, which generates an RGB image given a sketch only or both sketch and palette.

function for the GT palette based on the kernel \mathcal{K}_t and the stride \mathcal{J}_t). Similar to $\mathcal{F}_d(x_0, t)$ in the previous stage, larger t leads to more pixelation. Formulating the noise variance σ_t^2 using Eq. 6 could be interpreted as we have zero uncertainties at both edges of the bridge as we are sure where are in this domain, e.g., sketch or palette. In contrast, while moving away from a particular domain, the uncertainty increases until it reaches its maximum level in the middle, where we are not sure which domain we are.

3rd Stage: Detailed Image. The 3rd stage follows the same bridge formulation; however, the only difference is the starting point y . Consequently, it could start from the 1st output, i.e., the sketch, as shown in Figure 4, or by the fusion of the palette and the sketch as shown in Figure 1. Therefore, the forward function is as follows:

$$x_t = \alpha_t x_0 + (1 - \alpha_t) y + \sigma_t^2 \epsilon_t. \quad (7)$$

More details about the different starting points y are discussed in Section 4.2.

Training Objective & Reverse Process. We adapt the conventional diffusion models’ learning objective [18, 47], i.e., Variational Lower Bound (ELBO), Eq. 2, to include our new condition y , whereas, each marginal distribution has to be conditioned on y , as follows:

$$\begin{aligned} \mathcal{L}_{ELBO} = & -\mathbb{E}_q(D_{KL}(q(x_T|x_0, y)||p(x_T|y))) \\ & + \sum_{t=2}^T D_{KL}(q(x_{t-1}|x_t, x_0, y)||p_\theta(x_{t-1}|x_t, y)) \\ & - \log p_\theta(x_0|x_1, y)), \end{aligned} \quad (8)$$

where p_θ is a function approximator intended to predict from x_t . Using Bayes’ rule, we can formulate the reverse process as follows:

$$q(x_{t-1} | x_t, x_0, y) = \mathcal{N}(x_{t-1}; \tilde{\mu}(x_t, x_0, y), \tilde{\sigma}_t^2 \mathbf{I}) \quad (9)$$

$$\begin{aligned} \tilde{\mu}_t(x_t, x_0, y) = & \frac{\sigma_{t-1}^2}{\sigma_t^2} \frac{1 - \alpha_t}{1 - \alpha_{t-1}} x_t \\ & + (1 - \alpha_{t-1} (1 - \frac{\sigma_{t-1}^2 (1 - \alpha_t)^2}{\sigma_t^2 (1 - \alpha_{t-1})^2})) x_0 \\ & + (\alpha_{t-1} - \alpha_t \frac{1 - \alpha_t}{1 - \alpha_{t-1}} \frac{\sigma_{t-1}^2}{\sigma_t^2}) y \end{aligned} \quad (10)$$

$$\tilde{\sigma}_t^2 = \sigma_{t-1}^2 - \frac{\sigma_{t-1}^4}{\sigma_t^2} \frac{(1 - \alpha_t)^2}{(1 - \alpha_{t-1})^2} \quad (11)$$

The aforementioned equations are valid for the three stages, whereas the only difference is the x_0 formulation:

$$\tilde{x}_0 = \begin{cases} \mathcal{F}_d(x_0, t) & :i=1(\text{Abstract Contours}) \\ \mathcal{F}_p(x_0, \mathcal{K}_t, \mathcal{J}_t) & :i=2(\text{Palette}) \\ x_0 & :i=3(\text{Detailed Image}) \end{cases} \quad (12)$$

where i is the stage number. The derivation for Eq. 10 and Eq. 11 is in the supplementary materials. The overall training and sampling pipelines are summarized in Algorithms 1 and 2, respectively.

Algorithm 1 Training Pipeline

```

1: for  $i = 1, \dots, N$  do ▷ Train each stage separately
2:   for  $j = 1, \dots, E$  do ▷ Train for E epochs
3:     for  $(x_0, y) \in \mathcal{D}$  do ▷ Loop on the dataset  $\mathcal{D}$ 
4:        $\epsilon \in \mathcal{N}(0, I)$  ▷ Sampling the noise
5:        $t \in U(1, \dots, T)$  ▷ Sampling time-step
6:       Get  $\tilde{x}_0$  by applying Eq. 12 ▷  $\tilde{x}_0$  based on the stage
7:        $x_t = \alpha_t \tilde{x}_0 + (1 - \alpha_t) y + \sigma_t^2 \epsilon_t$  ▷ Forward process
8:        $\nabla_\theta \| \tilde{x}_0 - p_\theta(x_0|x_t, y) \|^2$  ▷ Simplified objective
9:     end for
10:   end for
11: end for

```

Algorithm 2 Sampling Pipeline

```

1:  $x_{inter} = []$  ▷ Initialize the list to save intermediate output for each stage
2:  $y_1 = \text{Zeros}((H, W, 1))$  ▷ Initialize 1st condition as a black image
3:  $\epsilon \in \mathcal{N}(0, I)$  ▷ Sampling the noise once
4: for  $i = 1, \dots, N$  do ▷ Sequential Sampling
5:    $x_T = y_i + \sigma_T^2 \epsilon_T$  ▷ Run forward process once
6:   for  $t = T, \dots, 1$  do ▷ Progressive Sampling
7:     Get  $x_{t-1}$  by applying Eq. 10:  $x_0^{(i)} = p_\theta(x_0|x_t)$  ▷ Reverse process
8:   end for
9:    $y_{i+1} = x_0^{(i)}$  ▷ Update the condition for the next stage
10:   $x_{inter}.append(x_0^{(i)})$  ▷ Store the intermediate outputs for each stage
11: end for
12: return  $x_{inter}$ 

```

3.2. Interpretability and Controllability

Our novel framework, ToddlerDiffusion (Figure 1), inherently provides interpretability and controllability. Algorithm 2 illustrates the generation of interpretable intermediate outputs at each stage N . This design not only allows users to monitor and understand the model’s generation process but also enhances debugging and editing capabilities. For instance, if an issue arises in a specific stage $n \in N$, such as the initial contour generation stage, users can interact with the system to edit the generated sketch S or bypass this stage by providing their input sketch. To maintain consistency between the edited version and the originally generated image, noise is sampled only once and fixed across all stages (Algorithm 2, line 3). Figure 2 showcases the editing capabilities of our framework. Starting from the generated sketch and RGB image (A), users can remove artifacts or undesired parts (B), add new content (C-D), and edit existing content (E-F) by manipulating the sketch.

3.3. Toddler Guidance

A crucial factor for the success of our framework, ToddlerDiffusion, lies in obtaining accurate and human-free guidance for the intermediate stages. Illustrated in Figure 1, the network progresses from generating contours to palette and ultimately uses both to produce the final image. To control error propagation across stages, accurate ground-truth contours and palettes are essential. Two modules, \mathcal{F}_s and \mathcal{F}_p , are employed to generate contours/sketches and palettes, respectively. The first module, $\mathcal{S} = \mathcal{F}_s(\mathcal{I})$, serves as a sketch or edge predictor, where $\mathcal{I} \in \mathbb{R}^{H \times W \times 3}$ is the ground-truth RGB image, and $\mathcal{S} \in \mathbb{R}^{H \times W \times 3}$ is the generated sketch. For instance, \mathcal{F}_s could be PidiNet [51] or Edter [42] for sketch generation, or Canny [4] and Laplacian [55] edge detectors. The palette can be obtained without human intervention by pixelating the ground-truth RGB image \mathcal{I} : $\mathcal{P} = \mathcal{F}_p(\mathcal{I}, \mathcal{K}, \mathcal{J})$, where $\mathcal{P} \in \mathbb{R}^{H \times W \times 3}$ is the pixelated image, and \mathcal{K} and \mathcal{J} are the kernel size and stride, respectively. This design choice is further analyzed in Section 4.2.

4. Experimental Results

Datasets. To probe the effectiveness of our proposed framework, ToddlerDiffusion, we conduct evaluations on two different datasets, i.e., unconditional, and text conditioning datasets, namely LSUN-Churches [58] and COCO [30]. LSUN-Churches [58] contains more than 120K images for outdoor buildings, mainly churches. COCO [30] is widely used for perception and generation tasks such, and it contains around 80K image-text pairs.

Network and Training Configuration. Our architecture comprises two key components: a denoising core network and an encoder-decoder for image-to-latent space transformation. We employ UNet [45] as the core network for de-

Method	VQGAN Parameters	Unet Parameters	FPS	Noise Scheduler	RGB FID ↓	Sketch FID ↓
a) LDM [44]	55.3	263	1	Linear	74.16	49
b) Ours	N/A	6.3 M	-	Bridge	89.21	269
c) Ours	N/A	6.3 M	-	Log	69.67	18.47
d) Ours	N/A	6.3 M	-	Linear	45.34	15.19

Figure 5. Ablation study for different representations for the 1st stage.

noising and VQGAN [11] as the image encoder-decoder. To tailor the architecture, we create four UNet variants (small, medium, large, and X-large) and three VQGAN variants (small, medium, and large), with detailed specifications available in the supplementary materials. Ablation studies are conducted from scratch for 50 epochs, using the weight initialization strategy from [17]. Following LDM [44], a fixed learning rate of 5×10^{-5} is used, while smaller UNet variants use 10^{-3} . Training employs the Adam optimizer [23] with a mini-batch size of 32 per GPU. While our architecture can consist of N stages, we explore three stages, as depicted in Figure 1: 1) Abstract structure, responsible for generating the contours. 2) Palette for generating the color scheme. 3) Detailed image, fine-grained image generation. For the abstract structure stage, we operate directly on the image space and use the smallest variant of UNet (S-UNet) due to its simplicity. For other stages, we operate in the latent space via using VQGAN-f4 [11]. Therefore, given an image $I \in \mathbb{R}^{256 \times 256 \times 3}$, we operate on latent-space $z \in \mathbb{R}^{64 \times 64 \times 3}$. Our framework is implemented in Python using the PyTorch framework and 8 Nvidia V100 GPUs.

4.1. 1st Stage: Abstract Structure

Sketch FID. A discrepancy exists between the reported conventional FID (RGB-FID), trained on ImageNet [8], and qualitative results, as illustrated in Figure 5. This discrepancy [14] may arise from differences between the training data (RGB images) and the evaluation data (binary images). To bridge this gap, we introduce Sketch-FID by re-training the inception model [52] on a sketch version of the ImageNet dataset. We generate sketches for ImageNet RGB images using PidiNet [51] and train the inception model on the conventional classification task.

Noise Scheduler. In the 1st stage, where our starting point y is a black image (Section 3.1), designing an appropriate noise scheduler is crucial. The bridge noise scheduler is intuitively unsuitable, as it eliminates randomness by adding no noise at both edges, fixing the starting point to a black image. This hypothesis is supported by empirical results in Figure 5, row b, where the model outputs random patterns. We explored linear and logarithmic schedulers, finding the linear schedule to be superior, yielding Sketch-FID scores of 15.19 and 18.47, respectively (Figure 5, rows c-d).

Ours Vs. LDM. In Section 3.1, we proposed an alternative

Input Type	FID ↓
a) Edges	9.5
b) Edges + Palette	8.4
c) Sketch	8.6
d) Sketch + Palette	7.2
e) SAM (Colored)	13.1
f) SAM (Edges)	8.1

Figure 6. Ablation study for different input’s types for the 2^{nd} stage.

to generating sketches by leveraging LDM [44], as shown in Figure 3, row A. However, this approach deviates from the nature of sketching. Our proposed formulation, aligned with the topology of sketches (Figure 3, row C), resulted in significant improvements over LDM in both model complexity and performance, as depicted in Figure 5. Our formulation (Section 3.1) allows direct operation on the image space (64×64) and compression of the Unet to a tiny variant without sacrificing performance. Despite the aggressive compression, our performance is significantly better than LDM, with respective Sketch-FID scores of 15.19 and 49, using a 41x smaller network.

4.2. Ablating 2^{nd} Stage Input Modalities

Contours Representation. In Section 3.3, we explore the versatility of the 3^{rd} stage (detailed image) by examining six input modalities, detailed in Figure 6. Comparing different contours representations, namely Edges (using Laplacian [55] edge detector), Sketch (utilizing PidiNet [51]), and SAM-Edges (generated by SAM [24] followed by Laplacian [55] edge detector), we find that Sketch outperforms Edges, as edges tend to be noisier. However, SAM-Edges provides more detailed contours, yielding superior results. Notably, feeding SAM-Colored leads to significant performance degradation, likely due to color discrepancies, as observed in SAM-1 and SAM-2 in Figure 6. While SAM-Edges achieves optimal results, its computational intensity renders it impractical. In contrast, Sketch and Edges are computationally inexpensive. Furthermore, the sparse and user-friendly nature of Sketch makes it more suitable for editing, facilitating interpretation and modification compared to dense, noisy edges. Consequently, we adopt Sketch as the input modality for subsequent experiments.

Palette Effect. Adding more guidance will offer more editing abilities to the pipeline and enhance the performance. As shown in Figure 6, rows b and d, when we incorporate the palette into the contours, i.e., edges and sketch, the performance improved by almost 1 and 1.5, respectively.

4.3. How to Fuse different Stages Efficiently?

The reported FID scores for the 1^{st} and the 2^{nd} stages, in Figure 5 and Figure 6, respectively, are for each stage separately. In other words, in Figure 6, row c, the 2^{nd} stage achieves an 8.6 FID score when a GT sketch is fed, which

Table 1. Ablation study showing the effect of the sketch augmentation on the overall performance after fusing the two stages, i.e., abstract and the detailed stages.

	Cutout [9] Percentage	Dropout Percentage	2^{nd} Stage FID ↓	Overall FID ↓
a)	0	0	8.6	16.10
b)	5-10	5-20	9.89	13.94
c)	10-20	20-40	9.77	13.98
d)	20-30	50-70	9.80	13.76
e)	30-40	70-90	11.68	17.99

Table 2. Systematic search for the best stopping step s for the condition truncation.

Metric/Steps (s)	0	10	20	40	80	120	160	200
2^{nd} stage FID ↓	7.1	7.4	7.9	8.6	9.9	10.4	10.8	11.2
Overall FID ↓	11.6	11.1	10.6	10.9	11.2	13.5	15.7	18.9

is obtained from PidiNet [51]. However, when we fed the generated sketch from the 1^{st} stage, the performance drastically dropped from 8.6 to 16.1 (almost doubled), as shown in Table 1, row a, due to the domain gap between the generated and the GT sketches. To fill this gap, we explored two types of augmentations: 1) Cutout and Dropout augmentation. 2) Condition truncation augmentation.

Cutout and Dropout Augmentation. First, we explored the straightforward augmentation types, such as Cutout [9] and Dropout augmentations. For the Cutout [9], we apply a kernel to randomly blackout patches in the sketch. Additionally, regarding the Dropout augmentation, we randomly convert white pixels to black pixels, interpreted as dropping some white points from the sketch. As shown in Table 1, generally, augmentation leads to a drop in the 2^{nd} stage performance while helping fill the gap in the overall performance, as the FID score decreased from 16 to almost 14. However, as shown in rows b-d, increasing the amount of the applied augmentation gradually does not help much, as the performance remains almost the same. However, the overall accuracy, i.e., FID, drops significantly from 14 to 18 when an aggressive augmentation is applied.

Condition Truncation Augmentation. As shown in Table 1, the conventional augmentation techniques do not help much. Accordingly, we explored another augmentation variant tailored for the diffusion models, i.e., condition truncation [19]. During training the 2^{nd} stage, we apply a random Gaussian noise to the fed condition, i.e., the sketch. So now the 2^{nd} stage is trained on noisy sketches instead of pure ones, which makes it more robust to the variations between the real sketches and the generated ones from the 1^{st} stage. Typically, we progressively generate the sketch in T time steps; $T \rightarrow 0$. However, This added noise could be interpreted as we stop the sketch generation (1^{st} stage) at a particular step s ; $T \rightarrow s$. Consequently, we search for it during sampling to determine which step s works best for the overall performance, as shown in Table 2. In other words, the 2^{nd} stage is trained on a wide range of perturbed sketches, e.g., pure sketch ($s = 0$), noisy one ($0 < s < T$),

Table 3. Comparing different variations of Unet and VQGAN architectures.

Architecture Name	Variant	N_{param}	Unet			Variant	VQGAN			1 Epoch Training Time (4*V100)	FID ↓	
			$N_{ResBlocks}$	Ch_{Mul}	Att_{Res}		N_{param}	$N_{ResBlocks}$	Ch_{Mul}		LDM	Ours
Small	Small	6.3 M	1	[1,1,1,1]	8	Small	2.8 M	1	[1,1,1]	7.5 Mins	36.20	30.21
Medium	Medium	69.5 M	2	[1,2,3,4]	8	Medium	15.1 M	2	[1,2,2]	10 Mins	17.85	16.52
Large	Large	101 M	3	[1,2,3,4]	8,4,2	Large	55.3 M	3	[1,2,4]	21 Mins	15.47	12.19
X-Large	X-Large	263 M	3	[1,4,8]	8,4,2	Large	55.3 M	3	[1,2,4]	33 Mins	15.19	10.63

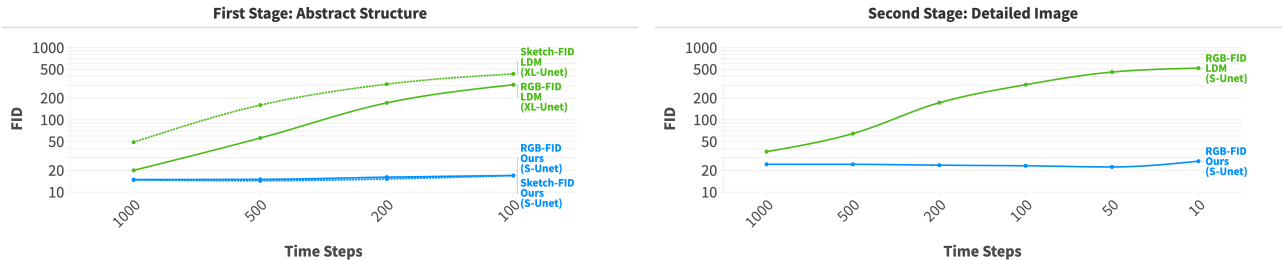


Figure 7. Ablation study for dropping the number of denoising steps needed during both training and sampling. On the left is the results for the first stage and on the right is the results for the second stage.

and even pure noise ($s = T$). The 1st stage is trained for 200 steps, so $s = 200$ means we omit the sketch and feed pure noise. In contrast, $s = 0$ indicates that we feed the generated sketch as it is to the 2nd stage. As shown in Table 2, following this truncation mechanism, the fusion of the two stages is performed more efficiently, where the overall performance drops from 16.1 to 10.6. Algorithm 2 is adapted in the supplementary materials to incorporate the condition truncation mechanism.

4.4. Flash Toddler

As shown in Algorithms 1 and 2, we have an additional loop over the stages N , which intuitively will lead to more slow down in the system. However, our approach is faster than the 1-stage vanilla LDM [44]. Our hypothesis is as follows: decomposing the complex generation problem into simpler steps could lead to: 1) Steps Trimming. 2) Slim Architecture. 3) Faster Convergence.

Steps Trimming. One key drawback of diffusion models is that they require enormous progressive time steps during sampling. In contrast, our framework, ToddlerDiffusion can drastically reduce the needed time steps during both training and sampling without requiring any additional post-processing tricks, such as DDIM [48] or step distillation [36, 46]. However, our framework is orthogonal with all these methods, and anyone could easily plug in and play with our architecture. To show this unique characteristic of our architecture, we deliberately drop the needed denoising steps for both stages, i.e., the abstract structure stage and the detailed image generation stage, during training and sampling. As shown in Figure 7, for both stages, when we reduce the number of training and sampling steps from 1000 to 100, our framework shows consistent and robust performance. In contrast, LDM’s performance [44] dropped dras-

tically. The reason why we can trim the denoising steps without significant impact on the performance, is maintaining a good SNR, especially for a large value of t , as discussed in detail in Section 3.1. Moreover, Figure 8 demonstrates another interesting ability of our framework. When we initially train the model using fewer denoising steps, it performs better than training it with larger steps, then use DDIM [48] or similar approaches to reduce the sampling steps. For instance, as shown in Figure 8, the green curve, which is trained using 100 steps, achieves around 60 FID scores when we use only ten steps during sampling. However, if we initially train the model on ten steps, as shown in yellow, it will perform much better: 15 FID.

Slim Architecture. By breaking down the complex task into simpler sub-tasks, we can use more efficient models for each stage. For instance, as discussed in Section 4.1, we outperform LDM’s performance by a significant margin while at the same time using a 41x smaller network. Moreover, we create four variants of the overall architecture by compressing both the VQGAN and the Unet architecture, as shown in Table 3. We detailed our analysis that leads to these four variations in the supplementary materials. Table 3 shows that our framework outperforms LDM across all architecture sizes. More interestingly, using only the large variant, we surpass the XL-LDM by a significant margin, where our FID score is 12.19, and LDM’s is 15.19. Consequently, using the medium variant, we achieve comparable results with XL-LDM while being 3x faster.

Faster Convergence. Sequentially tackling straightforward tasks and leveraging prior knowledge gained from the previous stage leads to a faster convergence rate, as demonstrated in Figure 9. Our approach surpasses the LDM performance trained for 20 epochs after only 10 epochs and outperforms the LDM performance after 50 epochs in just

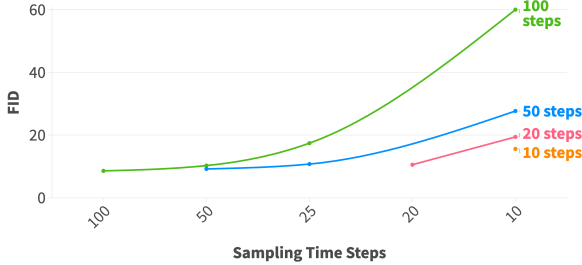


Figure 8. Training steps ablation study. The training steps are mentioned on the right of each curve, while the x-axis represents the sampling steps.

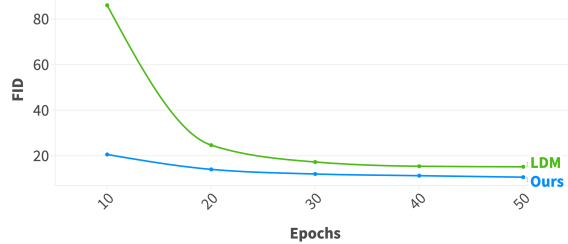


Figure 9. Comparing ToddlerDiffusion with LDM in terms of convergence rate.

Table 4. Benchmarking results on LSUN-Churches dataset [58]. We set the batch size to one, using only one V100 GPU while measuring the sampling speed (FPS). Our methods’ reported number of steps is only calculated for the RGB stage as the 1st stage uses 200 steps. However, the Unet architecture is too tiny; thus, its complexity footprint and run-time are negligible. Our results are obtained using only two stages, i.e., sketch and RGB stages.

Method	Editable	N_{Epochs}	1 Epoch Training Time (4*V100)	FPS	Sampling Steps	FID ↓	CLIP-FID ↓	KID ↓	Prec. ↑	Recall ↑
U-ViT [3]	✗	527	9Mins	0.088	1000	16.04	18.50	0.020	0.54	0.40
DiT [39]	✗	465	8.94Mins	0.474	1000	16.71	16.68	0.014	0.58	0.40
MDT [13]	✗	523	11.28Mins	0.661	1000	16.56	10.70	0.014	0.613	0.37
U-ViT [3]	✗	527	9Mins	1.60	50	20.04	20.60	0.022	0.48	0.41
DiT [39]	✗	465	8.94Mins	1.97	50	18.51	17.51	0.013	0.58	0.40
MaskDiT [59]	✗	506	9.07Mins	0.78	50	29.78	21.88	0.031	0.36	0.31
MDT [13]	✗	523	11.28Mins	1.67	50	19.49	11.81	0.015	0.61	0.37
LDM [44]	✗	50	33 Mins	1.28	50	15.16	17.3	0.009	0.59	0.39
ToddlerDiffusion (Ours)	✓	50	33 Mins	1.20	50	10.63	14.15	0.005	0.65	0.44
ToddlerDiffusion (Ours)	✓	50	33 Mins	1.80	20	12.11	15.66	0.007	0.64	0.37
LDM [44]	✗	50	33 Mins	3.13	10	31.5	26.85	0.023	0.36	0.19
ToddlerDiffusion (Ours)	✓	50	33 Mins	3.05	10	23.47	23.73	0.018	0.54	0.24

20 epochs, demonstrating its superiority. Additionally, the tailored methods for faster convergence [16] are orthogonal of our framework and can be easily integrated.

4.5. Comparison to State-of-the-art

We assess the effectiveness of our proposed framework, ToddlerDiffusion, on widely recognized benchmarks, namely LSUN-Churches [58], and COCO [30]. Due to space constraints, results for COCO are presented in the supplementary materials. By decomposing the generation task into interpretable stages, we outperform all efficient diffusion models operating on the latent space. Other methods with slow processing times are omitted for fairness, which would incur unfair comparisons due to their impractical sampling times. All methods in Table 4 were retrained to ensure a fair comparison, considering difficulties in reproducing and verifying LDM results¹. In Table 4, our method outperforms existing approaches by a significant margin. Notably, our FID score surpasses LDM by 4.5 and 6.5 points with 50 and 10 steps, respectively. This demonstrates our model’s ability to achieve superior performance

¹Refer to issues number 325, 262, 90, 142, 30, and 138 from the official LDM implementation.

not only with 50 steps but also under the more challenging constraint of using only ten sampling steps. The reported number of steps pertains only to the RGB stage, as the 1st stage employs 200 steps. However, the negligible complexity footprint and runtime of the tiny Unet architecture make it inconsequential. Our results are derived from two stages, namely the sketch and RGB stages.

5. Conclusion

In conclusion, we introduced a novel interpretable controllable diffusion model, ToddlerDiffusion, addressing key limitations in existing diffusion models. By decomposing the RGB generation task into interpretable stages inspired by the human generation system, our framework offers unprecedented editing and interaction capabilities for both conditional and unconditional generation. We showcased state-of-the-art results in challenging setups, surpassing all efficient diffusion-based methods in terms of training and sampling time, as well as overall performance. The inherent interpretability and efficiency of our approach mark a significant advancement in the synthesis and understanding of complex visual data.

References

- [1] Tobias Alt, Pascal Peter, and Joachim Weickert. Learning sparse masks for diffusion-based image inpainting. In *Iberian Conference on Pattern Recognition and Image Analysis*, pages 528–539. Springer, 2022. 1
- [2] Titas Anciukevičius, Zexiang Xu, Matthew Fisher, Paul Henderson, Hakan Bilen, Niloy J Mitra, and Paul Guerrero. Renderdiffusion: Image diffusion for 3d reconstruction, inpainting and generation. In *Proceedings of the IEEE/CVF Conference on Computer Vision and Pattern Recognition*, pages 12608–12618, 2023. 1
- [3] Fan Bao, Shen Nie, Kaiwen Xue, Yue Cao, Chongxuan Li, Hang Su, and Jun Zhu. All are worth words: A vit backbone for diffusion models. In *Proceedings of the IEEE/CVF Conference on Computer Vision and Pattern Recognition*, pages 22669–22679, 2023. 8
- [4] John Canny. A computational approach to edge detection. *IEEE Transactions on pattern analysis and machine intelligence*, (6):679–698, 1986. 5
- [5] Nicolas Carlini, Jamie Hayes, Milad Nasr, Matthew Jagielski, Vikash Sehwal, Florian Tramèr, Borja Balle, Daphne Ippolito, and Eric Wallace. Extracting training data from diffusion models. In *32nd USENIX Security Symposium (USENIX Security 23)*, pages 5253–5270, 2023. 1
- [6] Hyungjin Chung, Eun Sun Lee, and Jong Chul Ye. Mr image denoising and super-resolution using regularized reverse diffusion. *IEEE Transactions on Medical Imaging*, 42(4): 922–934, 2022. 1
- [7] Kamil Deja, Anna Kuzina, Tomasz Trzcinski, and Jakub Tomczak. On analyzing generative and denoising capabilities of diffusion-based deep generative models. *Advances in Neural Information Processing Systems*, 35:26218–26229, 2022. 2
- [8] Jia Deng, Wei Dong, Richard Socher, Li-Jia Li, Kai Li, and Li Fei-Fei. Imagenet: A large-scale hierarchical image database. In *2009 IEEE conference on computer vision and pattern recognition*, pages 248–255. Ieee, 2009. 5
- [9] Terrance DeVries and Graham W Taylor. Improved regularization of convolutional neural networks with cutout. *arXiv preprint arXiv:1708.04552*, 2017. 6
- [10] Prafulla Dhariwal and Alexander Nichol. Diffusion models beat gans on image synthesis. *Advances in neural information processing systems*, 34:8780–8794, 2021. 1
- [11] Patrick Esser, Robin Rombach, and Bjorn Ommer. Taming transformers for high-resolution image synthesis. In *Proceedings of the IEEE/CVF conference on computer vision and pattern recognition*, pages 12873–12883, 2021. 5
- [12] Sicheng Gao, Xuhui Liu, Bohan Zeng, Sheng Xu, Yanjing Li, Xiaoyan Luo, Jianzhuang Liu, Xiantong Zhen, and Baochang Zhang. Implicit diffusion models for continuous super-resolution. In *Proceedings of the IEEE/CVF Conference on Computer Vision and Pattern Recognition*, pages 10021–10030, 2023. 1
- [13] Shanghua Gao, Pan Zhou, Ming-Ming Cheng, and Shuicheng Yan. Masked diffusion transformer is a strong image synthesizer. *arXiv preprint arXiv:2303.14389*, 2023. 8
- [14] Songwei Ge, Vedanuj Goswami, C Lawrence Zitnick, and Devi Parikh. Creative sketch generation. *arXiv preprint arXiv:2011.10039*, 2020. 5
- [15] Kuang Gong, Keith Johnson, Georges El Fakhri, Quanzheng Li, and Tinsu Pan. Pet image denoising based on denoising diffusion probabilistic model. *European Journal of Nuclear Medicine and Molecular Imaging*, pages 1–11, 2023. 1
- [16] Tiankai Hang, Shuyang Gu, Chen Li, Jianmin Bao, Dong Chen, Han Hu, Xin Geng, and Baining Guo. Efficient diffusion training via min-snr weighting strategy. *arXiv preprint arXiv:2303.09556*, 2023. 8
- [17] Kaiming He, Xiangyu Zhang, Shaoqing Ren, and Jian Sun. Delving deep into rectifiers: Surpassing human-level performance on imagenet classification. In *Proceedings of the IEEE international conference on computer vision*, pages 1026–1034, 2015. 5
- [18] Jonathan Ho, Ajay Jain, and Pieter Abbeel. Denoising diffusion probabilistic models. *Advances in neural information processing systems*, 33:6840–6851, 2020. 1, 2, 3, 4
- [19] Jonathan Ho, Chitwan Saharia, William Chan, David J Fleet, Mohammad Norouzi, and Tim Salimans. Cascaded diffusion models for high fidelity image generation. *The Journal of Machine Learning Research*, 23(1):2249–2281, 2022. 6
- [20] Xuan Ju, Ailing Zeng, Chenchen Zhao, Jianan Wang, Lei Zhang, and Qiang Xu. Humansd: A native skeleton-guided diffusion model for human image generation. *arXiv preprint arXiv:2304.04269*, 2023. 3
- [21] Amirhossein Kazerooni, Ehsan Khodapanah Aghdam, Moein Heidari, Reza Azad, Mohsen Fayyaz, Ilker Hacıhaliloğlu, and Dorit Merhof. Diffusion models for medical image analysis: A comprehensive survey. *arXiv preprint arXiv:2211.07804*, 2022. 1
- [22] Diederik Kingma, Tim Salimans, Ben Poole, and Jonathan Ho. Variational diffusion models. *Advances in neural information processing systems*, 34:21696–21707, 2021. 3
- [23] Diederik P Kingma and Jimmy Ba. Adam: A method for stochastic optimization. *arXiv preprint arXiv:1412.6980*, 2014. 5
- [24] Alexander Kirillov, Eric Mintun, Nikhila Ravi, Hanzi Mao, Chloe Rolland, Laura Gustafson, Tete Xiao, Spencer Whitehead, Alexander C Berg, Wan-Yen Lo, et al. Segment anything. *arXiv preprint arXiv:2304.02643*, 2023. 6
- [25] Vladimir Kulikov, Shahar Yadin, Matan Kleiner, and Tomer Michaeli. Sinddm: A single image denoising diffusion model. In *International Conference on Machine Learning*, pages 17920–17930. PMLR, 2023. 1
- [26] Bo Li, Kaitao Xue, Bin Liu, and Yu-Kun Lai. Bbdlm: Image-to-image translation with brownian bridge diffusion models. In *Proceedings of the IEEE/CVF Conference on Computer Vision and Pattern Recognition*, pages 1952–1961, 2023. 2, 3
- [27] Haoying Li, Yifan Yang, Meng Chang, Shiqi Chen, Huajun Feng, Zhihai Xu, Qi Li, and Yueting Chen. Srdiff: Single image super-resolution with diffusion probabilistic models. *Neurocomputing*, 479:47–59, 2022. 1
- [28] Yanyu Li, Huan Wang, Qing Jin, Ju Hu, Pavlo Chemerys, Yun Fu, Yanzhi Wang, Sergey Tulyakov, and Jian Ren. Snapfusion: Text-to-image diffusion model on mobile devices

- within two seconds. *arXiv preprint arXiv:2306.00980*, 2023. [1](#)
- [29] Zheng Li, Yuxuan Li, Penghai Zhao, Renjie Song, Xiang Li, and Jian Yang. Is synthetic data from diffusion models ready for knowledge distillation? *arXiv preprint arXiv:2305.12954*, 2023. [1](#)
- [30] Tsung-Yi Lin, Michael Maire, Serge Belongie, James Hays, Pietro Perona, Deva Ramanan, Piotr Dollár, and C Lawrence Zitnick. Microsoft coco: Common objects in context. In *Computer Vision–ECCV 2014: 13th European Conference, Zurich, Switzerland, September 6–12, 2014, Proceedings, Part V 13*, pages 740–755. Springer, 2014. [2](#), [5](#), [8](#)
- [31] Guan-Horng Liu, Tianrong Chen, Oswin So, and Evangelos Theodorou. Deep generalized schrödinger bridge. *Advances in Neural Information Processing Systems*, 35:9374–9388, 2022. [3](#)
- [32] Cheng Lu, Yuhao Zhou, Fan Bao, Jianfei Chen, Chongxuan Li, and Jun Zhu. Dpm-solver: A fast ode solver for diffusion probabilistic model sampling in around 10 steps. *Advances in Neural Information Processing Systems*, 35:5775–5787, 2022. [1](#)
- [33] Andreas Lugmayr, Martin Danelljan, Andres Romero, Fisher Yu, Radu Timofte, and Luc Van Gool. Repaint: Inpainting using denoising diffusion probabilistic models. In *Proceedings of the IEEE/CVF Conference on Computer Vision and Pattern Recognition*, pages 11461–11471, 2022. [1](#)
- [34] David Marr. On the purpose of low-level vision. 1974. [1](#)
- [35] David Marr. *Vision: A computational investigation into the human representation and processing of visual information*. MIT press, 2010. [1](#)
- [36] Chenlin Meng, Robin Rombach, Ruiqi Gao, Diederik Kingma, Stefano Ermon, Jonathan Ho, and Tim Salimans. On distillation of guided diffusion models. In *Proceedings of the IEEE/CVF Conference on Computer Vision and Pattern Recognition*, pages 14297–14306, 2023. [7](#)
- [37] Alexander Quinn Nichol and Prafulla Dhariwal. Improved denoising diffusion probabilistic models. In *International Conference on Machine Learning*, pages 8162–8171. PMLR, 2021. [1](#)
- [38] Maury FM Osborne. Brownian motion in the stock market. *Operations research*, 7(2):145–173, 1959. [3](#)
- [39] William Peebles and Saining Xie. Scalable diffusion models with transformers. In *Proceedings of the IEEE/CVF International Conference on Computer Vision*, pages 4195–4205, 2023. [8](#)
- [40] Ben Poole, Ajay Jain, Jonathan T Barron, and Ben Mildenhall. Dreamfusion: Text-to-3d using 2d diffusion. *arXiv preprint arXiv:2209.14988*, 2022. [1](#)
- [41] Konpat Preechakul, Nattanat Chatthee, Suttisak Widadwongsa, and Supasorn Suwajanakorn. Diffusion autoencoders: Toward a meaningful and decodable representation. In *Proceedings of the IEEE/CVF Conference on Computer Vision and Pattern Recognition*, pages 10619–10629, 2022. [1](#)
- [42] Mengyang Pu, Yaping Huang, Yuming Liu, Qingji Guan, and Haibin Ling. Edter: Edge detection with transformer. In *Proceedings of the IEEE/CVF conference on computer vision and pattern recognition*, pages 1402–1412, 2022. [5](#)
- [43] Guocheng Qian, Jinjie Mai, Abdullah Hamdi, Jian Ren, Aliaksandr Siarohin, Bing Li, Hsin-Ying Lee, Ivan Skokhodov, Peter Wonka, Sergey Tulyakov, et al. Magic123: One image to high-quality 3d object generation using both 2d and 3d diffusion priors. *arXiv preprint arXiv:2306.17843*, 2023. [1](#)
- [44] Robin Rombach, Andreas Blattmann, Dominik Lorenz, Patrick Esser, and Björn Ommer. High-resolution image synthesis with latent diffusion models. In *Proceedings of the IEEE/CVF conference on computer vision and pattern recognition*, pages 10684–10695, 2022. [3](#), [5](#), [6](#), [7](#), [8](#)
- [45] Olaf Ronneberger, Philipp Fischer, and Thomas Brox. U-net: Convolutional networks for biomedical image segmentation. In *Medical Image Computing and Computer-Assisted Intervention–MICCAI 2015: 18th International Conference, Munich, Germany, October 5–9, 2015, Proceedings, Part III 18*, pages 234–241. Springer, 2015. [5](#)
- [46] Tim Salimans and Jonathan Ho. Progressive distillation for fast sampling of diffusion models. *arXiv preprint arXiv:2202.00512*, 2022. [7](#)
- [47] Jascha Sohl-Dickstein, Eric Weiss, Niru Maheswaranathan, and Surya Ganguli. Deep unsupervised learning using nonequilibrium thermodynamics. In *International conference on machine learning*, pages 2256–2265. PMLR, 2015. [1](#), [2](#), [4](#)
- [48] Jiaming Song, Chenlin Meng, and Stefano Ermon. Denoising diffusion implicit models. *arXiv preprint arXiv:2010.02502*, 2020. [1](#), [7](#)
- [49] Yang Song, Jascha Sohl-Dickstein, Diederik P Kingma, Abhishek Kumar, Stefano Ermon, and Ben Poole. Score-based generative modeling through stochastic differential equations. *arXiv preprint arXiv:2011.13456*, 2020. [1](#), [2](#)
- [50] Kent A Stevens. The vision of david marr. *Perception*, 41(9):1061–1072, 2012. [1](#)
- [51] Zhuo Su, Wenzhe Liu, Zitong Yu, Dewen Hu, Qing Liao, Qi Tian, Matti Pietikäinen, and Li Liu. Pixel difference networks for efficient edge detection. In *Proceedings of the IEEE/CVF international conference on computer vision*, pages 5117–5127, 2021. [5](#), [6](#)
- [52] Christian Szegedy, Wei Liu, Yangqing Jia, Pierre Sermanet, Scott Reed, Dragomir Anguelov, Dumitru Erhan, Vincent Vanhoucke, and Andrew Rabinovich. Going deeper with convolutions. In *Proceedings of the IEEE conference on computer vision and pattern recognition*, pages 1–9, 2015. [5](#)
- [53] Roy Voetman, Maya Aghaei, and Klaas Dijkstra. The big data myth: Using diffusion models for dataset generation to train deep detection models. *arXiv preprint arXiv:2306.09762*, 2023. [1](#)
- [54] Gefei Wang, Yuling Jiao, Qian Xu, Yang Wang, and Can Yang. Deep generative learning via schrödinger bridge. In *International Conference on Machine Learning*, pages 10794–10804. PMLR, 2021. [2](#), [3](#)
- [55] Xin Wang. Laplacian operator-based edge detectors. *IEEE transactions on pattern analysis and machine intelligence*, 29(5):886–890, 2007. [5](#), [6](#)
- [56] Julia Wolleb, Florentin Bieder, Robin Sandkühler, and Philippe C Cattin. Diffusion models for medical anomaly

- detection. In *International Conference on Medical image computing and computer-assisted intervention*, pages 35–45. Springer, 2022. [1](#)
- [57] Junde Wu, Huihui Fang, Yu Zhang, Yehui Yang, and Yanwu Xu. Medsegdiff: Medical image segmentation with diffusion probabilistic model. *arXiv preprint arXiv:2211.00611*, 2022. [1](#)
- [58] Fisher Yu, Ari Seff, Yinda Zhang, Shuran Song, Thomas Funkhouser, and Jianxiong Xiao. Lsun: Construction of a large-scale image dataset using deep learning with humans in the loop. *arXiv preprint arXiv:1506.03365*, 2015. [2](#), [5](#), [8](#)
- [59] Hongkai Zheng, Weili Nie, Arash Vahdat, and Anima Anandkumar. Fast training of diffusion models with masked transformers. *arXiv preprint arXiv:2306.09305*, 2023. [8](#)
- [60] Yuanzhi Zhu, Kai Zhang, Jingyun Liang, Jiezhong Cao, Bihan Wen, Radu Timofte, and Luc Van Gool. Denoising diffusion models for plug-and-play image restoration. In *Proceedings of the IEEE/CVF Conference on Computer Vision and Pattern Recognition*, pages 1219–1229, 2023. [1](#)